

FINAL REPORT

NASA Research Contract NAS-36955 DO 126

Period of Performance

6/24/91 - 9/04/93

**MODELLING OF THE MEA FLOAT ZONE
USING ACCELEROMETER DATA**

PREPARED BY:

J. IWAN D. ALEXANDER (Principal Investigator)

**Center for Microgravity and Materials Research
The University of Alabama in Huntsville
Huntsville, Alabama 35899**

1. Introduction

During a floating zone experiment involving the growth of indium on a recent orbiter mission, (STS 32) oscillation of the zone shapes were observed to occur in response to the background acceleration. An understanding of the nature of the response of the zone shape to forced (g-jitter) oscillations and predictions of its impact on future experiments is of great interest not only to the PI's of but to other commercial and academic investigators who plan to fly similar experiments in the orbiter and on space station. Motivated by this, a 15 month study was undertaken to analyze the nature of the g-sensitivity of the STS 32 floating zone crystal growth experiment. Numerical models were used to describe the time-dependent free surface motion of the zone as it responds to the spacecraft residual acceleration. Relevant experimental data concerning the acceleration environment was obtained from the Honeywell in Space Accelerometer (HISA) investigators through MSFC's ACAP program and processed and analyzed. For the indium floating zone experiment a series of calculations were made using time-dependent axial accelerations $g(t)$. The form of $g(t)$ included simple sinusoidal disturbances as well as actual data (subject to appropriate filtering) measured on the STS 32 mission. The study focused the calculation of the response of the free surface of the zone as well as the internal flows and internal heat transfer. The influence of solidification on the response of the zone shape was also examined but found to be negligible.

The results are summarized in section 3 and details are supplied in the appendix. In section 4, published papers and presentations given that involve this work are listed. References are given in section 5.

2. Background

Zhang and Alexander [1] have approached the problem of determining the axisymmetric response of the shape of the free surface of a cylindrical liquid column bounded by two solid regions is modelled by 1-D system of non-linear equations. It is found that the sensitivity of the zone shape depends on the static Bond number, B_o , aspect ratio and viscosity as well as the amplitude and frequency of the disturbance. The general trend is an increase in tolerable residual gravity with increasing frequency. At the eigenfrequencies of the zone, however, there are dramatic deviations from this trend. At these frequencies the tolerable residual gravity level can be two orders of magnitude lower at this frequency. Aspect ratios ranging from 96.3 to 82.7% of the Rayleigh limit were examined. For these cases, the frequencies associated with the lowest tolerable acceleration have been found in the 10^{-2} - 10^{-1} Hz range. In terms of previously recorded and predicted residual accelerations the sensitive frequency ranges for the cases examined are 10^{-2} - 10^{-1} Hz and 1-10 Hz. Maximum tolerable residual gravity levels as low as 10^{-6} g have been calculated. The effect of viscosity is seen to increase the tolerable acceleration level for all frequencies. The equilibrium shape, as determined by the steady background acceleration, has a pronounced effect at low frequencies. A change in slenderness of the bridge markedly changes the sensitivity to residual acceleration as the Rayleigh limit is approached.

To assess the influence of g-jitter on thermocapillary flow it is useful to consider the dimensionless groups involved. The dimensionless groups associated with mixed thermocapillary convection and buoyancy-driven convection are [2]:

The Dynamic Bond number:	$Bd = \rho g L^2 / \gamma_T$
The Marangoni number:	$Ma = \gamma_T \Delta T L / \mu \kappa$
The Grashof number	$G_r = \Delta T \beta g L^3 / \nu^2$
The Prandtl number	$Pr = \nu / \kappa$
The Surface Reynolds number	$R_s = Ma Pr^{-1}$,

Here ρ is the liquid density, $\gamma_T = d\gamma/dT$, μ and ν are the shear and kinematic viscosities of the fluid melt, g is the acceleration, L is some characteristic length scale, ΔT is a characteristic temperature difference and κ is the liquid's thermal diffusivity.

The relative importance of gravity and thermocapillary forces can be estimated as follows [2,3]:

First, the velocity reference scale is obtained from a consideration of the balance of force tangent to the free surface [2]

$$-\mu \frac{\partial \tilde{u}}{\partial x} = \frac{\partial \gamma}{\partial z} = |\gamma_T| \frac{\partial \tilde{T}}{\partial z}. \quad (1)$$

If the velocity and temperature are scaled by V and ΔT , and lengths are scaled by L , then (1) can be recast as

$$-\frac{\partial u}{\partial x} = \left(\frac{|\gamma_T| \Delta T}{\mu V^*} \right) \frac{\partial \theta}{\partial z}, \quad (2)$$

where u and θ represent the dimensionless velocity and temperature, and x and z are the dimensionless lengths.

For terms on both sides of (2) to be of the same order the magnitude of V^* must be [2,3]

$$V^* = \frac{|\gamma_T| \Delta T}{\mu}. \quad (3)$$

The balance of linear momentum and energy in a Boussinesq fluid are given by

$$\frac{\partial \tilde{\mathbf{v}}}{\partial t} + (\text{grad} \tilde{\mathbf{v}}) \tilde{\mathbf{v}} = -\frac{1}{\rho} \text{grad} \tilde{p} + \nu \Delta \tilde{\mathbf{v}} + \beta_T \tilde{T} \mathbf{g}(\tilde{t}). \quad (4)$$

For steady flows Ostrach [2] used (3) to scale (4). For an aspect ratio of 1 and with $R_s \ll 1$ he obtained:

$$\Delta \mathbf{v} = -\text{grad} p + \frac{G_r}{R_s} \mathbf{g}(t), \quad (5)$$

where the pressure is scaled with $\mu V^*/L$.

For $R_s \gg 1$ a boundary layer scale, $\delta = L/\sqrt{R_s}$, was employed to scale the coordinate perpendicular to the free surface. For this steady boundary layer situation the component of (4) perpendicular to the interface has the (dimensionless) form

$$u \frac{\partial v}{\partial x} + v \frac{\partial v}{\partial y} = -R_s^{2/3} \frac{\partial p}{\partial y} + \frac{1}{R_s^{2/3}} \frac{\partial^2 v}{\partial x^2} + \frac{\partial^2 v}{\partial y^2} + \frac{G_r}{R_s} \mathbf{g}(t), \quad (6)$$

At small values of R_s the relative contribution of the buoyancy force to convection can be estimated from the ratio G_r/R_s . For large values of R_s , the relative importance of buoyancy is found upon comparing the buoyancy term with the pressure gradient and is expressed via the ratio $G_r/R_s^{2/3}$.

In order to estimate the effect of time-dependent periodic accelerations on a thermocapillary flow we adopt the approach of Langbein and Tiby and express the magnitude of the velocity caused by an acceleration occurring with a circular frequency ω as

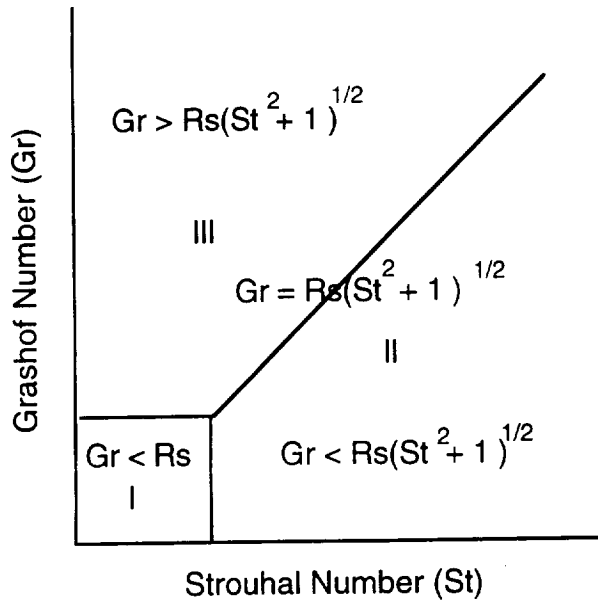


Fig. 1 Sensitivity regimes for thermocapillary flow expressed in terms of the Grashof (Gr), Strouhal (St) and surface Reynolds (Rs) numbers. After Alexander [3].

For thermocapillary flow to dominate, the ratio of V_g to V^* must be less than one. For this to occur the magnitude of the periodic acceleration must satisfy:

$$V_g \approx \frac{L^2 \beta_T \Delta T g}{(\omega^2 + \frac{v^2}{L^4})^{1/2}}, \quad (7)$$

Equation (7) can be re-interpreted in terms of the ratio of the Grashof number, Gr, and the surface Reynolds number R_s . The condition that buoyancy and thermocapillary forces are of the same magnitude is [3]

$$G_r = R_s (S_t^2 + 1)^{1/2}, \quad (8)$$

where $S_t = \omega L^2 / \nu$ is the Strouhal number. This condition is illustrated graphically in Fig. 1. Three regimes of interest are identified. These regions are defined by the relative values of the Grashof, Strouhal and surface Reynolds numbers. In region I, the Strouhal number S_t is less than one, and the condition that thermocapillary forces dominate is equivalent to that for a steady flow. In region II, S_t is greater than one. In this region, for a fixed value of R_s , the value of Gr required to give buoyancy forces equal weight to thermocapillary forces increases with increasing values of the Strouhal number. This essentially reflects the fact that the characteristic time for the fluid response greatly exceeds the period of the disturbance. Thus, thermocapillary forces dominate at higher values of than in region I. In region III buoyancy forces predominate over thermocapillary forces.

Alexander [3] estimated the sensitivity of surface-tension-driven flow to residual acceleration for a number of different thermocapillary flow systems (under the assumption that the free surface would not deform). In general, these estimates suggest that periodic vibrations (with amplitudes and frequencies characteristic of spacelab) will generally not lead to significant buoyancy effects except in extreme cases. These estimates are confirmed by our numerical modelling. For cases where one or more of the boundaries are deformable, the density

difference across that boundary determines the extent to which g-jitter induced motion of the surface will influence the internal flow in the liquid. For the case under investigation here, the interface motion can, as we shall see in the next section and in appendix I, dominate the flow (depending on the frequency and amplitude of the g-jitter).

More recent work by Zhang and Alexander [4] involving full axisymmetric calculations indicates that the isothermal 1D model give a reliable indication of the frequency dependence of the shape sensitivity for isothermal and some non-isothermal flows. The full numerical models are, however, essential for a description of the internal flow and heat transfer (especially in the non-isothermal cases).

During a floating zone experiment involving the growth of indium on a recent orbiter mission STS 32, oscillation of the zone shapes were observed to occur in response to the background acceleration. In addition to these observed oscillations, zone lengths in excess of the often quoted Rayleigh limit [5,6] were recorded. The Rayleigh limit occurs when the length of the zone exceeds 2π times its radius and is associated with the tendency of the surface tension of the liquid to cause the zone to break up. Zone lengths in excess of this limit can be explained in several ways, including melt volumes in excess of the right circular cylindrical volume corresponding to the zone length and feed rod radius, by surface contamination resulting in zero surface tension, highly non-planar boundaries separating the solid indium from the indium melt (causing stabilization due to the large deviation of the zone shape from a circular cylinder), or by the stabilizing action of surface-driven (thermocapillary) flow [7]. Regardless of the mechanism by which these excessively long zones were achieved, the response of the zone shape to forced (g-jitter) oscillations is of great interest not only to the PI's of but to other commercial and academic investigators who plan to fly similar experiments in the orbiter and on space station.

3. *The model floating zone*

Governing equations

A full numerical model of the axisymmetric free surface response of a non-isothermal liquid subject to axial vibration was employed. We assume that the surface tension of the melt varies linearly with temperature. Thus, the presence of a temperature gradient along the free surface of the liquid bridge gives rise to a thermocapillary flow.

Consider a cylindrical liquid zone (see Fig. 2) held between two parallel coaxial circular rigid disks (radius = R_0) separated by a distance L . The liquid is a non-isothermal incompressible Newtonian fluid. The bridge is held between the disks by surface tension. The free surface of the bridge is a gas-liquid interface and is described by $r=R(z,t)$. Each disk is maintained at a constant temperature T_0 . Surface heating is provided through a function, $T_\infty(z)$, which represents the heater profile. The heat transfer coefficient at the free surface is denoted by h . In addition, we make the assumptions that the residual acceleration is parallel to the cylinder axis and the velocity and temperature field and the deformation of free surface are axisymmetric. Furthermore, we let the surface tension at the free surface vary linearly with temperature and assume that the Boussinesq approximation holds.

The governing equations are made dimensionless by scaling length, time and velocity with R_0 , R_0^* and U^* respectively. Here U^* is a characteristic velocity given by

$$U^* = \frac{|\gamma|\Delta T}{\mu},$$

where $\Delta T = T_{\max} - T_{\min}$ represents the maximum temperature difference at the surface, $|\gamma|$ is the absolute value of the derivative of the surface tension with respect to temperature, and μ is the dynamic viscosity.

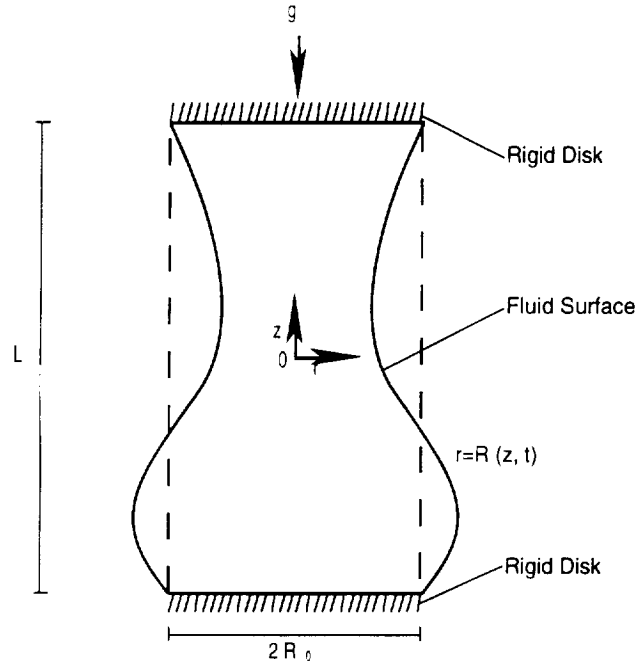


Figure 2. The Model Floating Zone

The temperature maximum in a floating zone occurs between the two ends of the zone. We shall take T_{\max} to be $T_{\infty}(0)$, and T_{\min} to be T_0 , where $\Lambda = L_0$ is the aspect ratio.

The non-dimensional pressure is

$$p = \frac{p^* + \rho_0 g^*(t) z}{\rho_0 U^{*2}} R_0$$

where p^* is the dimensional pressure, $g^*(t)$ is the residual gravitational acceleration, z is the dimensionless axial coordinate and ρ_0 is the density corresponding to the reference temperature. The temperature is rendered dimensionless using $T_{\max} - T_{\min}$. With these scales the dimensionless equations in a cylindrical coordinate system can be written as

$$\frac{1}{r} \frac{\partial(ru)}{\partial r} + \frac{\partial w}{\partial z} = 0, \quad (1)$$

$$\frac{\partial u}{\partial t} + u \frac{\partial u}{\partial r} + w \frac{\partial u}{\partial z} = -\frac{\partial p}{\partial r} + \frac{1}{\text{Re}} \left(\frac{\partial^2 u}{\partial r^2} + \frac{1}{r} \frac{\partial u}{\partial r} + \frac{\partial^2 u}{\partial z^2} - \frac{u}{r^2} \right), \quad (2)$$

$$\frac{\partial w}{\partial t} + u \frac{\partial w}{\partial r} + w \frac{\partial w}{\partial z} = -\frac{\partial p}{\partial z} + \frac{1}{\text{Re}} \left(\frac{\partial^2 w}{\partial r^2} + \frac{1}{r} \frac{\partial w}{\partial r} + \frac{\partial^2 w}{\partial z^2} \right) + \frac{\text{Gr}}{\text{Re}^2} T g(t), \quad (3)$$

$$\frac{\partial T}{\partial t} + u \frac{\partial T}{\partial r} + w \frac{\partial T}{\partial z} = \frac{1}{\text{Ma}} \left(\frac{\partial^2 T}{\partial r^2} + \frac{1}{r} \frac{\partial T}{\partial r} + \frac{\partial^2 T}{\partial z^2} \right), \quad (4)$$

where $g(t)$ is a time-dependent dimensionless residual acceleration, and the Reynolds number, Re , Marangoni number, Ma and Grashof number Gr are, respectively,

$$\text{Re} = \frac{R_0 U^*}{\nu}, \quad \text{Ma} = \frac{|\gamma| \Delta T R_0}{\mu \kappa}, \quad \text{Gr} = \frac{|g^*| \beta \Delta T R_0^3}{\nu^2}.$$

Here, ν is the kinematic viscosity, κ is the thermal diffusivity, β is the volume thermal expansion and coefficient, and $|g^*|$ is the (maximum) residual acceleration magnitude

Boundary Conditions

At the ends of the zone, the boundary conditions are

$$u = T = 0, \quad w = w^+(t), \quad \text{at } z = \pm \frac{\Lambda}{2}, \quad (5)$$

where $w^+(t)$ is zero if the two rigid disks vibrate in phase (this will admit only odd mode deformations of the zone surface [1]). The symmetry conditions at the centerline $r = 0$ are

$$u = \frac{\partial w}{\partial r} = \frac{\partial T}{\partial r} = 0, \quad (6)$$

The boundary conditions at the free surface $r=R(z)$ take the form

$$p - Gg(t)z + \lambda = \frac{2R_e^{-1}}{1 + \left(\frac{\partial R}{\partial z}\right)^2} \left[\frac{\partial u}{\partial r} + \left(\frac{\partial R}{\partial z}\right)^2 \frac{\partial w}{\partial z} - \frac{\partial R}{\partial z} \left(\frac{\partial w}{\partial r} + \frac{\partial u}{\partial z} \right) \right] + \frac{Re^{-1} (C_0^{-1} - T)}{\left[1 + \left(\frac{\partial R}{\partial z}\right)^2 \right]^{3/2}} \left[\frac{1 + \left(\frac{\partial R}{\partial z}\right)^2}{R} - \frac{\partial^2 R}{\partial z^2} \right], \quad (7)$$

$$\left[1 - \left(\frac{\partial R}{\partial z}\right)^2 \right] \left(\frac{\partial u}{\partial z} + \frac{\partial w}{\partial r} \right) + 2 \frac{\partial R}{\partial z} \left(\frac{\partial u}{\partial r} - \frac{\partial w}{\partial z} \right) = - \left[1 + \left(\frac{\partial R}{\partial z}\right)^2 \right]^{1/2} \left(\frac{\partial T}{\partial z} + \frac{\partial R}{\partial z} \frac{\partial T}{\partial r} \right), \quad (8)$$

$$\frac{\partial R}{\partial t} + u + w \frac{\partial R}{\partial z} = 0, \quad (9)$$

$$\frac{1}{\left(1 + \left(\frac{\partial R}{\partial z}\right)^2 \right)^{1/2}} \left(\frac{\partial T}{\partial r} - \frac{\partial R}{\partial z} \frac{\partial T}{\partial z} \right) + Bi(T - T_\infty) = 0 \quad (10)$$

Where

$$C_0 = \frac{\gamma \Delta T}{\gamma_0}, \quad Bi = \frac{hR_0}{\kappa}, \quad G = \frac{gR_0}{U^{*2}}$$

and are, respectively, the capillary number, Biot number, dimensionless gravitational acceleration and γ_0 is the mean surface tension and κ is thermal conductivity. The force balance at the free surface in the normal and tangential directions are given by eqs. (7) and (8), respectively. Equation (9) is the kinematic boundary condition at the liquid-gas interface. The thermal boundary condition at the interface is given by equation (10) in which the equivalent heat transfer coefficient h contains the effect of the radiant and convective heat transfer. The constant λ in (7) represents a dimensionless reference pressure difference² across the interface. In model liquid bridge systems with fixed rigid endwalls such as the one discussed here λ is determined by the following constant volume constraint

$$V = \int_{-\frac{\Lambda}{2}}^{\frac{\Lambda}{2}} \pi R^2(z) dz = V_0 \equiv \text{constant}. \quad (11)$$

Finally, the condition that the contact lines between the liquid end disks are fixed is

$$R = 1 \text{ at } z = \pm \Lambda/2. \quad (12)$$

Numerical method

The governing equations are recast in terms of a vorticity stream function together with a non-orthogonal coordinate transformation. The latter allows an irregular free boundary to coincide with a coordinate line (or surface) without the need to solve a coupled set of Laplace equations. The resulting equations are discretized following a pseudo-unsteady semi-implicit difference scheme and solved by the A.D.I. method. The combination of the above methods provides a very accurate and economical solution procedure. Generally, the tangential stress condition and kinematic condition at the free surface are solved along with the Navier-Stokes and continuity equations. The normal force balance condition is used to determine the free surface shape. In addition, an "outer" iterative procedure is needed to locate the free surface.

The unsteady free boundary problem for cylindrical liquid zone is solved as follows. First the initial conditions are specified. We shall use initial conditions corresponding to either zero residual acceleration or a steady residual acceleration. These states will be calculate using a method similar to that described below but designed specifically for the computation of steady solutions. A Picard iterative procedure [8] is then followed:

1. Guess the free surface shape for the new time step;
2. Obtain the approximate temperature and velocity fields by transforming the governing equations and boundary conditions to a circular cylindrical domain via a non-orthogonal transformation and solve them using a pseudo-unsteady semi-implicit method;
3. Obtain the pressure at the free surface by integrating the transformed momentum equation;
4. Use the normal force balance condition at free surface to decide how to update the free surface location;
5. Return to step 2. Repeat until convergence is obtained by satisfying all equations and boundary conditions to a specified degree of accuracy for this time step.

Non-orthogonal Transformation

The region occupied by the liquid zone is transformed into a fixed cylindrical computational region (see Fig. 2) using a non-orthogonal coordinate transformation, i.e.

$$\eta = z, \quad \xi = \frac{r}{R(z)} \quad (17)$$

This transforms the domain

$$-\frac{\Lambda}{2} < z < \frac{\Lambda}{2}, \quad 0 < r < R(z),$$

onto the rectangle.

$$-\frac{\Lambda}{2} < z < \frac{\Lambda}{2}, \quad 0 < r < R(z),$$

It then follows that

$$\frac{\partial}{\partial r} \rightarrow \frac{1}{R} \frac{\partial}{\partial \zeta}, \quad \frac{\partial}{\partial z} \rightarrow \frac{\partial}{\partial \eta} - \frac{\zeta}{R} \frac{\partial R}{\partial \eta} \frac{\partial}{\partial \zeta}. \quad (18)$$

The advantage of this transformation is that the free boundary coincides exactly with a coordinate line in a computational grid and regeneration of mesh during the outer iteration is avoided.

We have checked our method by comparing our results with those of Hyer et al. [9] has been made. The convergence of the solution was also checked by varying the spatial resolution of the mesh. This was particularly important at higher values of Re , where, owing to the space-centered-differences [10] the stream function was prone to exhibit “wiggles” if the grid Peclet number exceeded 2 in the vicinity of the disks. As observed by Ryskin and Leal [11], an increase in the mesh resolution was found to eliminate this problem. Thus, the use of upwind differencing, and consequent loss of accuracy [10,11], to avoid this problem was not necessary.

4. Results

The results of our calculations are summarized in this section. More details and the results of our analysis of the HISA data are given in the appendices.

The sensitivity of an indium float zone was analyzed using the 2D model described earlier. The input accelerations used ranged from a simple sinusoidal disturbance to a disturbance synthesized from an the Honeywell In-space accelerometer. Our studies indicate that the components of the disturbance with frequencies around 2.5 -4 Hz results in the greatest response for any given acceleration amplitude. This is because the eigenfrequency of the zone examined is 3.4 Hz. Figure 6 in appendix I shows a set of sensitivity curves for an indium zone which shows the enhanced sensitivity of the bridge to vibration in the vicinity of the bridge eigenfrequencies. This result is in qualitative agreement with surface motions observed on video taken of the zone on STS-52, and also agrees with our results simulated from HISA data which shows a peak acceleration associated with 3 frequencies in the 1-5 Hz range. The largest peak corresponds to 2.7 Hz and is associated with use of the treadmill (see appendix II). The other two peaks are associated with structural modes and correspond to 1.8 Hz and 3.5 Hz. The maximum tolerable amplitude to produce a significant observable deformation of the bridge surface was exceeded about 39% of the time that HISA was operational. More details on the acceleration history are given in appendix II.

5. Publications, papers presented at conferences and students graduated

Publications

- J.I.D. Alexander, H. Cordier, J. Ouazzani and Y. Zhang, "Numerical Simulation of Thermocapillary flow under Zero and Low Gravity Conditions," AIAA Paper no. 93-0254, 31st Aerospace Sciences Meeting, Reno, Nevada, 1993.
- M.J.B. Rogers, J.I.D. Alexander and J. Schoess, Detailed Analysis of the Honeywell In-space Accelerometer- STS 52," Microgravity Science and Technology, VI, 28-33, 1993.
- J.I.D. Alexander and Y.Q. Zhang, "The Sensitivity of a Nonisothermal Liquid Bridge to Residual Acceleration," Microgravity Science and Technology, IV, 128-129, 1991. *extended abstract; Full article in: Microgravity Fluid Mechanics, ed. H.J. Rath, Proceedings of the IUTAM Symposium, Bremen, Germany (Springer Verlag, Berlin, 1991) pp. 167-174.

Papers presented

- "Analysis of Experiment Sensitivity to Residual Acceleration", International Symposium on Microgravity Science and Application, Beijing, China, May 10-12, 1993

- “Modelling or Muddling? Analysis of Buoyancy Effects on Transport under Low Gravity Conditions,” presented at the World Space Congress, Washington D.C. August 28-September 5, 1992.
- “Numerical Simulation of Thermocapillary Flow Under Zero and Low Gravity Conditions” presented at the AIAA 31st Annual Aerospace Science Meeting, Reno, Nevada, USA. Jan. 11-14, 1993
- “Detailed Analysis of the Honeywell In-Space Accelerometer Data STS-32”, (poster) presented at the World Space Congress, Washington D.C. August 28-September 5, 1992.
- “The Sensitivity of a Nonisothermal Liquid Bridge to Residual Acceleration,” 5th Annual Alabama Materials Research Conference, September 25-26 1991, Birmingham, Alabama.
- “The Sensitivity of a Nonisothermal Liquid Bridge to Residual Acceleration,” IUTAM Symposium on Microgravity Fluid Mechanics, September 2-6, 1991 Bremen, Germany.
- “Numerical Analysis of the Effects of Low Gravity on Convection and Transport,” Case Western Reserve University, Department of Mechanical Engineering, February 6th, 1992.
- “Numerical Simulation of Low-g Fluid Transport”, AIAA Short Course on Low-Gravity Fluid Mechanics, January 10-12, 1992, Reno, Nevada

Students graduated

Helene Cordier, M.S. Mechanical Engineering, 1993.

6. *References*

- [1] Y. Q. Zhang and J. I. D. Alexander, “Sensitivity of liquid bridges subject to axial residual acceleration”, *Physics of Fluids* **A2** (1990) 1966.
- [2] S. Ostrach, *Ann. Rev. Fluid Mech.*, **14** (1982) 313.
- [3] J. I.D. Alexander, *Microgravity Science and Technology*, **III** (1990) 2.
- [4] Y. Q. Zhang and J. I. D. Alexander, unpublished research, Center for Microgravity and Materials Research, University of Alabama in Huntsville.
- [5] Lord Rayleigh, *Proc. Royal. Soc.*, **29** (1879) 71.
- [6] A. D. Myshkis, V. G. Babskii, N. D. Kopachevskii, L. A. Slobozhanin and A. D. Typutsov, *Low Gravity Fluid Mechanics* (Springer Verlag, Berlin, 1987) pg. 198, and references therein.
- [7] J.-J. Xu and S. H. Davis, *J. Fluid Mechanics*, **161** (1985) 1.
- [8] J. M. Floryan, *Appl. Mech. Rev.* **42** (1989) 323.
- [9] J. Hyer, D.F. Jankowski and G.P. Neitzel, “Thermo-capillary convection in a model float zone, to be published *AIAA Journal of Thermophysics and Heat Transfer*, 1990.
- [10] R. Peyret and T. D. Taylor, *Computational Methods for Fluid Flow*, Springer Verlag, New York (1983) pg. 28.
- [11] G. Ryskin and L. G. Leal, “Numerical solution of free boundary problems in fluid mechanics. Part 1. The finite-difference technique.” *J. Fluid Mech.* **148** (1984) 1.

Appendix I

The sensitivity of a non-isothermal liquid bridge to residual acceleration

J. Iwan D. Alexander and Yiqiang Zhang

Center for Microgravity and Materials Research

University of Alabama in Huntsville, Huntsville, Alabama 35899, USA

Abstract

Liquid bridges appear in a variety of industrial processes, for example in the well-known floating-zone crystal growth technique. This crystal growth method has received much attention in recent years. In particular, there have been a variety of experiments on spacelab missions. These experiments are motivated by the fact that the microgravity environment affords the possibility of an increase in the stability of the melt meniscus and a reduction in buoyancy-driven convection. However, within the spacecraft there is a residual acceleration with variable magnitude and orientation. Under certain conditions, the response of the free surface of a liquid bridge to time-dependent residual accelerations will lead to zone breakage. In this paper the steady and unsteady behavior of isothermal and non-isothermal liquid bridge systems under normal and low gravity conditions is examined. The full non-linear governing equations are recast in terms of a stream-function vorticity formulation together with a non-orthogonal coordinate transformation. The latter allows an irregular free boundary to coincide with a coordinate line (or surface) without the need to solve a coupled set of Laplace equations. The resulting equations are discretized using a centered finite difference scheme for space, and an Adams-Bashforth-Crank-Nicolson scheme is used for time. The equations are solved by the A.D.I. method and a Picard type iteration is used on the boundary condition for the balance of force normal to the free surface. For non-isothermal bridges, residual acceleration affects the system by causing internal buoyancy flows and fluctuations in the shape of the bridge which interact with the thermocapillary flow caused by surface tension gradients. For the cases examined, the shape of the bridge is found to be more sensitive to typical spacecraft accelerations than the buoyancy driven flow. The effect of thermocapillary flow on the surface shape is found to be small for the range of capillary and Reynolds numbers considered.

1. Introduction

Liquid bridges appear in a variety of industrial processes, for example the well-known floating-zone crystal growth technique [1]. This crystal growth method has received much attention in recent years [2-10]. In particular, there have been several related experiments on spacelab missions [11-14]. These experiments are motivated by the fact that the microgravity environment affords the possibility of an increase in the stability of the melt meniscus and a reduction in buoyancy-driven convection. However, within the spacecraft there is a residual acceleration with variable magnitude and orientation. Under certain conditions, the response of the free surface of an isothermal liquid bridge to time-dependent residual accelerations will lead to zone breakage [13-15]. In this paper we examine the interaction between convection caused by the response of the free surface of the zone to oscillatory axial residual acceleration and convection due to thermocapillary and internal buoyancy forces.

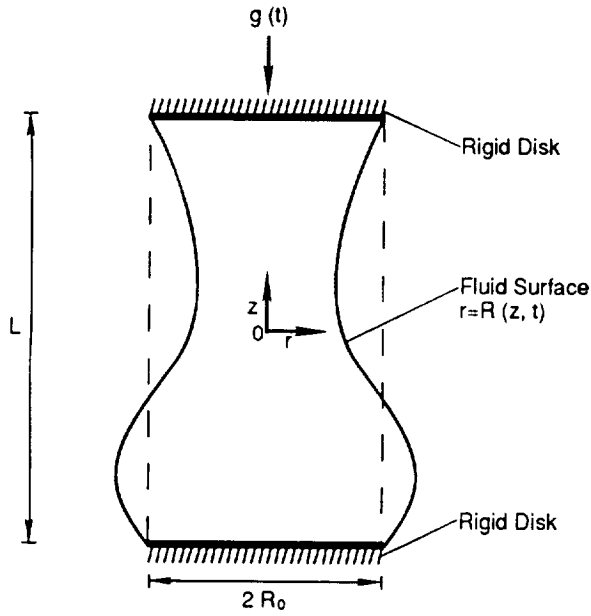


Fig. 1. The model liquid bridge.

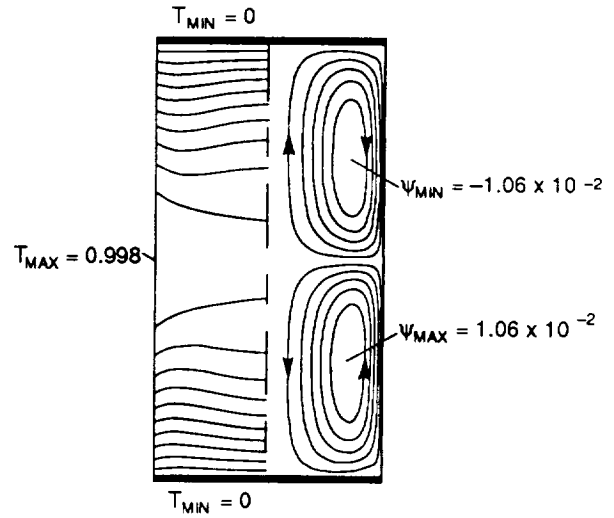


Fig. 2. The initial steady dimensionless stream-function and temperature corresponding to $Re = 2899$, $Gr = 0.98$, $\Lambda = 4$ and $Pr = 0.0127$.

2. Formulation

2.1 Description of the Model

A cylindrical liquid zone (see Fig. 1) is contained between two parallel coaxial circular rigid disks (radius = R_0) separated by a distance L . The liquid is a non-isothermal Newtonian fluid for which the Boussinesq approximation holds. The bridge is held between the disks by surface tension. The free surface of the bridge is a gas-liquid interface and is described by $r = R(z, t)$. Each disk is maintained at a constant temperature \tilde{T}_0 . Surface heating is provided through a parabolic function, \tilde{T}_∞ , which is a function of the axial coordinate and is an approximation to the heating profile associated with typical floating zone crystal growth experiments. The heat transfer coefficient at the free surface is denoted by h . In addition, we make the assumptions that the residual acceleration is parallel to the cylinder axis, the velocity and temperature field and the deformation of free surface are axisymmetric, and we take the surface tension at the free surface to be a linear function of the temperature. Motion of the end disks perpendicular to the axis may also occur in practice. The restriction to axial acceleration precludes an analysis of the effects of such motions.

The governing equations are made dimensionless by scaling length, time and velocity with R_0 , R_0/U^* and U^* , respectively. Here U^* is a characteristic velocity given by

$$U^* = \frac{|\gamma_T| \Delta \tilde{T}}{\mu},$$

where $\Delta \tilde{T} = \tilde{T}_{MAX} - \tilde{T}_{MIN}$ represents the maximum temperature difference along the surface, $|\gamma_T|$ is the absolute value of the derivative of the surface tension with respect to temperature, and μ is the

dynamic viscosity. The difference ΔT is used to non-dimensionalize temperature.

The temperature maximum in a floating zone occurs between the two ends of the zone. We shall take the dimensionless ambient temperature T_{MAX} to be $T_\infty(0)$, and T_{MIN} to be $T_\infty(\pm\Lambda/2)$, where $\Lambda = L/R_0$ is the aspect ratio.

The non-dimensional pressure is

$$p = \frac{p^* + \rho_0 g^*(t) z}{\rho_0 U^{*2}} R_0,$$

where p^* is the dimensional pressure, z is the dimensionless axial coordinate, ρ_0 is the density corresponding to the reference temperature and $g^*(\tilde{t}) = g_0 + g_1 \sin(2\pi f\tilde{t})$ is the residual gravitational acceleration.

2.2 Basic Equations

With the scales presented in 2.1 the governing dimensionless equations in a cylindrical coordinate system can be written as

$$\frac{1}{r} \frac{\partial(ru)}{\partial r} + \frac{\partial w}{\partial z} = 0, \quad (1)$$

$$\frac{\partial u}{\partial t} + u \frac{\partial u}{\partial r} + w \frac{\partial u}{\partial z} = -\frac{\partial p}{\partial r} + \frac{1}{Re} \left(\frac{\partial^2 u}{\partial r^2} + \frac{1}{r} \frac{\partial u}{\partial r} + \frac{\partial^2 u}{\partial z^2} - \frac{u}{r^2} \right), \quad (2)$$

$$\frac{\partial w}{\partial t} + u \frac{\partial w}{\partial r} + w \frac{\partial w}{\partial z} = -\frac{\partial p}{\partial z} + \frac{1}{Re} \left(\frac{\partial^2 w}{\partial r^2} + \frac{1}{r} \frac{\partial w}{\partial r} + \frac{\partial^2 w}{\partial z^2} \right) + \frac{Gr}{Re^2} T g(t), \quad (3)$$

$$\frac{\partial T}{\partial t} + u \frac{\partial T}{\partial r} + w \frac{\partial T}{\partial z} = \frac{1}{Ma} \left(\frac{\partial^2 T}{\partial r^2} + \frac{1}{r} \frac{\partial T}{\partial r} + \frac{\partial T}{\partial z^2} \right), \quad (4)$$

where $g(t) = g^*(\tilde{t})/g_0$ is a time-dependent dimensionless residual acceleration, and

$$Re = \frac{R_0 U^*}{\nu}, \quad Ma = \frac{|\gamma_T| \Delta T R_0}{\mu \kappa}, \quad Gr = \frac{|g_0| \beta \Delta T R_0^3}{\nu^2},$$

are, respectively, the Reynolds number, Marangoni number and Grashof number. Here, ν is the kinematic viscosity, κ is the thermal diffusivity, β is the volume thermal expansion and coefficient.

The boundary conditions at the rigid end disks are

$$u = T = 0, \quad w = w^\pm(t), \quad \text{at } z = \pm \frac{\Lambda}{2}, \quad (5)$$

where $w^\pm(t)$ is zero if the two disks vibrate in phase (this will admit only odd mode deformations of the zone surface [15]). The symmetry conditions at the centerline $r = 0$ are

$$u = \frac{\partial w}{\partial r} = \frac{\partial T}{\partial r} = 0, \quad (6)$$

The boundary conditions at the free surface $r = R(z)$ take the form

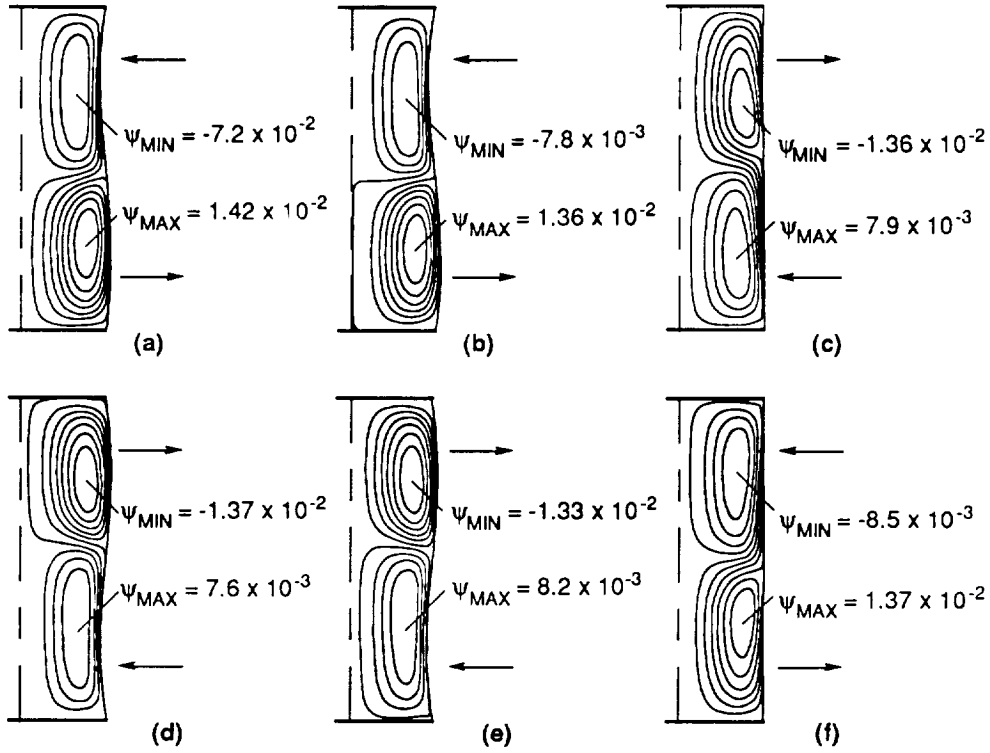


Fig. 3. The instantaneous dimensionless stream-functions with $Re = 2899$, $Gr = 0.98$, $\Lambda = 4$ and $Pr = 0.0127$, at (a) 0.52 s, (b) 0.59 s, (c) 1 s, (d) 1.5 s, (e) 1.56 s, (f) 2 s, after application of an additional $2.5 \times 10^{-2} g$, 0.5 Hz, axial acceleration.

$$p - \frac{g(t)z}{F^2} + \lambda = \frac{2Re^{-1}}{1 + \left(\frac{\partial R}{\partial z}\right)^2} \left[\frac{\partial u}{\partial r} + \left(\frac{\partial R}{\partial z}\right)^2 \frac{\partial w}{\partial z} - \frac{\partial R}{\partial z} \left(\frac{\partial w}{\partial r} + \frac{\partial u}{\partial z} \right) \right] + \frac{Re^{-1}(C_0^{-1} - T)}{\left[1 + \left(\frac{\partial R}{\partial z}\right)^2\right]^{\frac{3}{2}}} \left[\frac{1 + \left(\frac{\partial R}{\partial z}\right)^2}{R} - \frac{\partial^2 R}{\partial z^2} \right], \quad (7)$$

$$\left[1 - \left(\frac{\partial R}{\partial z}\right)^2 \right] \left(\frac{\partial u}{\partial z} + \frac{\partial w}{\partial r} \right) + 2 \frac{\partial R}{\partial z} \left(\frac{\partial u}{\partial r} - \frac{\partial w}{\partial z} \right) = - \left[1 + \left(\frac{\partial R}{\partial z}\right)^2 \right]^{\frac{1}{2}} \left(\frac{\partial T}{\partial z} + \frac{\partial R}{\partial z} \frac{\partial T}{\partial r} \right), \quad (8)$$

$$\frac{\partial R}{\partial t} + u + w \frac{\partial R}{\partial z} = 0, \quad (9)$$

$$\left(1 + \left(\frac{\partial R}{\partial z}\right)^2 \right)^{\frac{1}{2}} \left(\frac{\partial T}{\partial r} - \frac{\partial R}{\partial z} \frac{\partial T}{\partial z} \right) + Bi(T - T_{\infty}) = 0, \quad (10)$$

where the capillary number, Biot number and Froude number are, respectively,

$$C_0 = \frac{\gamma_T |\Delta T|}{\gamma_0}, \quad Bi = \frac{hR_0}{k}, \quad F = \left(\frac{gR_0}{U^*2} \right)^{-\frac{1}{2}},$$

and γ_0 is the mean surface tension and k is the thermal conductivity. The force balance conditions normal and tangent to the free surface are given by eqs. (7) and (8) respectively. Equation (9) is the kinematic boundary condition at the liquid-gas interface. The thermal boundary condition at the interface is given by equation (10) in which the equivalent heat transfer coefficient, h , models the effect of the radiant and convective heat transfer between the bridge and the surrounding environment. The constant λ in (7) represents a dimensionless reference pressure difference across the interface which for this system is determined by the following constant volume constraint [9,16]

$$V = \int_{-\frac{\Lambda}{2}}^{\frac{\Lambda}{2}} \pi R^2(z) dz = V_0 \equiv \text{constant} . \quad (11)$$

Finally, the condition that the contact lines between the liquid end disks are fixed is

$$R = 1 \text{ at } z = \pm \Lambda/2. \quad (12)$$

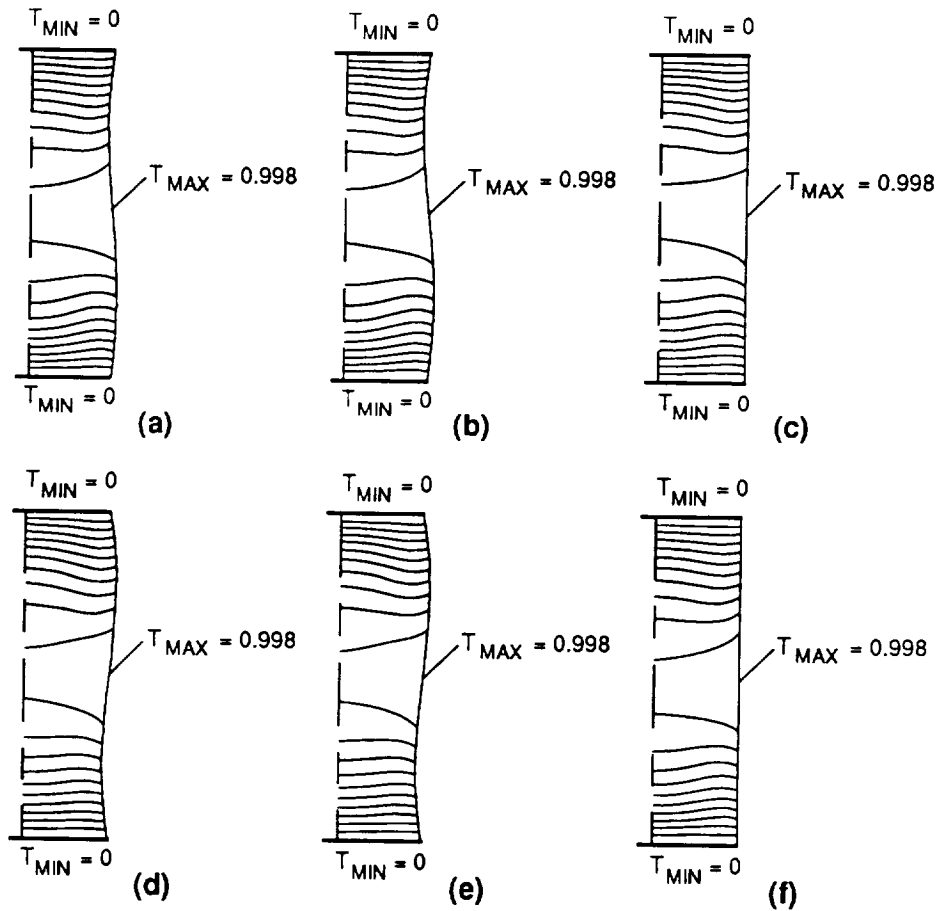


Fig. 4. The dimensionless temperature field with $Re = 2899$, $Gr = 0.98$, $\Lambda = 4$ and $Pr = 0.0127$, at (a) 0.52 s, (b) 0.59 s, (c) 1 s, (d) 1.5 s (e) 1.56 s, (f) 2 s, after application of an additional $2.5 \times 10^{-2} g$, 0.5 Hz, axial acceleration.

2.3 Solution Method

In the present investigation, the governing equations are recast in terms of a stream-function vorticity formulation. The stream-function is defined by

$$u = \frac{1}{r} \frac{\partial \Psi}{\partial z}, \quad v = -\frac{1}{r} \frac{\partial \Psi}{\partial r}. \quad (13)$$

A non-orthogonal coordinate transformation,

$$\eta = z, \quad \xi = \frac{r}{R(z,t)}, \quad (14)$$

allows an irregular free boundary to coincide with a cylindrical coordinate line (or surface) without the need to solve a coupled set of Laplace equations [17,18]. The resulting equations are discretized following a semi-implicit difference scheme and solved by the A.D.I. method. The conditions for force balance tangent to the surface and kinematic condition at the free surface are solved along with the Navier-Stokes and continuity equations. The condition for the force balance normal to the surface is used together with an “outer” iterative procedure to determine the free surface shape.

The unsteady free boundary problem for a cylindrical liquid zone is solved as follows. The

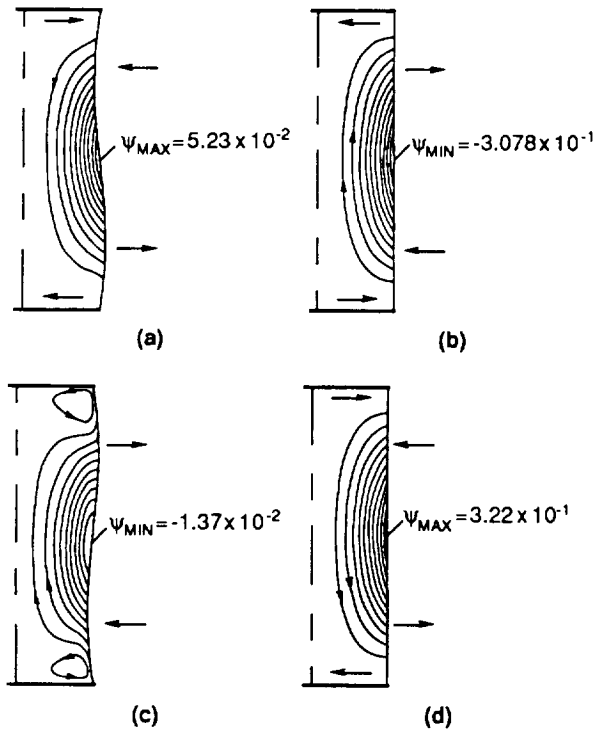


Fig. 5. The instantaneous dimensionless stream-function, with $Re = 0$, $Gr = 0$, $\Lambda = 4$ and $Pr = 0.0127$, at (a) 0.59 s, (b) 1 s, (c) 1.5 s (e) 2 s, after application of an additional 2.5×10^{-2} g, 0.5 Hz, axial acceleration. Note that for this case only, $\Psi = \Psi / \kappa R_0$, where Ψ is the dimensional stream-function $\text{cm}^3 \text{s}^{-1}$.

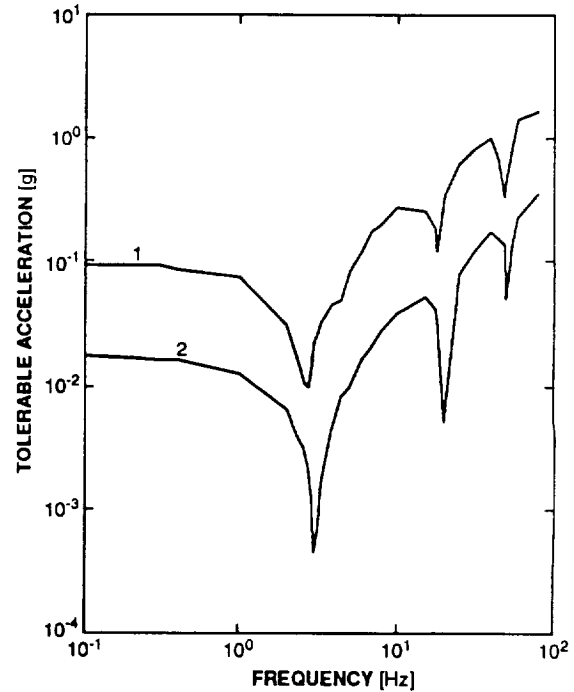


Fig. 6. Tolerable acceleration [g] vs. Frequency [Hz] predicted by the 1D model [15] for (1) breakage and (2) 10% shape change, for an isothermal liquid zone with $\Lambda = 4$ and the thermophysical properties of indium.

initial conditions correspond to either zero or finite steady residual acceleration situations with a steady thermocapillary flow. These states are calculated using a method close to that described below [16]. For the unsteady calculation our solution scheme is similar to that used by Kang and Leal [17] and Ryskin and Leal [18]. The following Picard iterative procedure [19] is adopted:

1. guess the free surface shape for the new timestep;
2. obtain the approximate temperature and stream-function, vorticity and velocity fields by transforming the governing equations and boundary conditions to a circular cylindrical domain via a non-orthogonal transformation and solve them using a semi-implicit method;
3. obtain the pressure at the free surface by integrating the transformed momentum equation;
4. use the condition for the balance of force normal to the free surface to decide how to update the free surface location;
5. return to step 2. Repeat until convergence is obtained by satisfying all equations and boundary conditions to a specified degree of accuracy for this timestep.

3. Results and Discussion

The following results were obtained for a liquid zone corresponding to the physical properties of molten indium subject to an axial acceleration with a frequency of 0.5 Hz. Fig. 2 depicts the initial state of the system. A steady axial acceleration of magnitude $10^{-4} g$ ($10^{-3} m s^{-2}$) acts along the negative z -direction. Two equidimensional toroidal rolls indicate that surface-driven flow is dominant ($Re = 2899$, $Gr = 0.98$). The isotherm distribution shows that heat transfer is mainly by conduction, although some distortion of the isotherms by the flow is evident. For indium, Lind [20] has reported that the surface tension increases with increasing temperature i.e. $\gamma_T > 0$. (Note that surface contamination may have affected the measured temperature dependence of surface tension in this case.) Thus, the flow direction at the surface is toward the center (i.e. the higher temperature region). Figs. 3 and 4 illustrate the effect of an additional acceleration component which varies sinusoidally with a frequency of 0.5 Hz. Figure 5 depicts the response of the zone to the same disturbance, but with $Gr = Ma = 0$. (Note that, for this case, κ/L rather than $|\gamma_T| \Delta T / \mu$ was used as the velocity scale.) In another case with $Re = 2899$, $Gr = 0.98$ and the surface constrained to be a circular cylinder, no observable response occurred. Clearly the system is more sensitive to the effects of free surface motion than internal buoyancy. Given that the value of steady acceleration used is extreme for spacecraft acceleration environments [21], we may conclude that for systems where internal buoyancy-driven effects are not manifested (in this case because they are swamped by the surface-driven flow) it suffices to examine the response of the free surface only. Furthermore, a comparison of our full axisymmetric results with those obtained with a simplified 1D isothermal model indicates that, at least for the conditions examined, the 1D model may be used to reliably predict liquid zone (isothermal and nonisothermal) sensitivity. The 1D model is described in detail in [15]. Fig. 6 shows the sensitivity of an indium liquid zone to axial acceleration. The curves are based on results obtained using two sensitivity criteria. The first is determined by

breakage of the bridge, the second is whenever the bridge shape changes by more than 10% of its static shape, i.e. $R(z,t) - R(z,0) = .1R(z,0)$.

Acknowledgements

This work was supported by the State of Alabama through the Center for Microgravity and Materials Research and the Alabama Supercomputer Network, and by the National Aeronautics and Space Agency through grant NAG8-724.

4. References

- [1] W.G. Pfann, *Zone Melting*, Krueger, Huntington New York (1978).
- [2] C. Chang and W.R. Wilcox, *J. Crystal Growth* **28**, 8-12 (1975).
- [3] P.A. Clark and W.R. Wilcox, *J. Crystal Growth* **50**, 461-469 (1980).
- [4] N. Kobayashi, *J. Crystal Growth* **66**, 63-72 (1984).
- [5] W.W. Fowlis and G.O. Roberts, *J. Crystal Growth* **74**, 301-320 (1986).
- [6] A. Rybicki and J.M. Floryan, *Phys. Fluids* **30**, 1956-1972 (1987).
- [7] R. Natarjan, *AIChE J.* **35**, 614-624 (1989).
- [8] Z. Kozhoukharova and S. Slavchev, *J. Crystal Growth* **74**, 236-246 (1986).
- [9] J.L. Duranceau and R.A. Brown, in Taylor G. Wang (ed.) *Drops and Bubbles Third International Colloquium 1988*, AIP Conference Proceedings **197**, American Institute of Physics, New York, 1989, pp. 133-144.
- [10] C.W. Lan and S. Kou, *J. Crystal Growth* **102**, 609-627 (1990).
- [11] D.T.J. Hurle, G. Müller and R. Nitsche, in *Fluid Sciences and Materials Science in Space*, Ed. H. U. Walter (Springer Verlag, Berlin, 1987) pp. 313-351.
- [12] A. Cröll, W. Müller and R. Nitsche, *Proceedings of the 6th European Symposium on Materials Sciences under Microgravity Conditions*, **ESA SP-256** (ESA Publications Division, Noordwjyck, 1987) 87.
- [13] I. Martinez, J.M. Haynes and D. Langbein, in *Fluid Sciences and Materials Science in Space*, Ed. H. U. Walter (Springer Verlag, Berlin, 1987) pp. 53-80.
- [14] I. Martinez, *Proceedings of the 6th European Symposium on Materials Sciences under Microgravity Conditions*, **ESA SP-256** (ESA Publications Division, Noordwjyck, 1987) 235.
- [15] Y.Q. Zhang and J.I.D. Alexander, *Physics of Fluids A* **2**, 1966 (1990).
- [16] Y.Q. Zhang and J.I.D. Alexander, *International Journal for Numerical Methods in Fluids* in press.
- [17] I.S. Kang and L.G. Leal, *Physics of Fluids* **30**, 1929-1940 (1987).
- [18] G. Ryskin and L.G. Leal, *J. Fluid Mech.* **148**, 1-17 (1984).
- [19] J.M. Floryan, *Appl. Mech. Rev.* **42**, 323-341 (1989).
- [20] M.D. Lind, *Proceedings of the AIAA 25th Aerospace Sciences Meeting, Reno, Nevada*, AIAA-87-0618 (1987).
- [21] J.I.D. Alexander, *Microgravity Science and Technology* **3**, 52 (1990).

Appendix II

M. J. B. Rogers, J. I. D. Alexander, and J. Schoess

Detailed Analysis of Honeywell In-space Accelerometer Data - STS-32

SEE ALSO
93A32070

The Honeywell In-Space Accelerometer system (HISA) collected data in the mid-deck area of the Shuttle Columbia during the flight of STS-32, January 1990. The resulting data were to be used to investigate the response of crystal microstructure to different types of residual acceleration. The HISA, using Sundstrand QA-2000 sensors, is designed to detect and record transient and oscillatory accelerations. The sampling and electronics package stored averaged accelerations over two sampling periods; two sampling rates were available: 1 Hz and 50 Hz. Analysis of the HISA data followed the CMMR Acceleration Data Processing Guide, considering in-house computer modelling of a float-zone indium crystal growth experiment. Characteristic examples of HISA data showing the response to the primary reaction control system (PRCS), Orbiter Maneuvering System (OMS) operations and crew treadmill activity are presented. Various orbiter structural modes are excited by these and other activities. Such modes are in the 1 Hz to 20 Hz range. Of particular note is the distinct frequency of crew footfalls during exercise periods and the resultant excitation of orbiter frequencies. Acceleration vector magnitudes ranged from 10^{-4} g to $>10^{-2}$ g. Acceleration values recorded at the crystal growth site exceeded time domain tolerance limits in approximately 35% of the data, especially during PRCS firings, OMS burns, and treadmill exercise. Frequency domain limits, however, were not exceeded.

1 Introduction

The Honeywell In-Space Accelerometer system (HISA) collected data on the mid-deck of the Space Shuttle Columbia during the flight of STS-32, January 1990. The HISA was part of the Microgravity Disturbances Experiment (MDE) which also included the Rockwell Fluids Experiment Apparatus (FEA). The FEA is a float-zone materials processing furnace; for this flight, it was used to grow single crystals of metallic indium. At various times during growth, acceleration sources were activated in order to investigate the response of crystal microstructure to different types of

Mail address: Melissa J. B. Rogers, J. Iwan D. Alexander, Center for Microgravity and Materials Research, University of Alabama in Huntsville, Huntsville AL 35899, USA; Jeff Schoess, Honeywell Inc., Bloomington MN 55420, USA.

residual acceleration. The HISA acceleration measurements are presented and discussed herein.

In sect. 2 we outline the MDE location and HISA operation in the orbiter mid-deck. Sect. 3 discusses our processing plan, based on estimated acceleration sensitivities. In sect. 4 we present and discuss time history and frequency domain plots of segments of the HISA data. These data are compared to data from other missions in sect. 5 and suggestions are made for revisions of the HISA system before its further use in low-gravity environments.

2 Experiment Set-up

We present here a brief overview of the MDE; more detailed discussions can be found in Schoess [1] and Dunbar et al. [2]. During operation the MDE was mounted at locker MA9F in the aft mid-deck of Columbia. Crew members observed and videotaped the shape changes of the liquid indium zone. Post flight crystal characterization was planned to investigate crystallographic defects and impurity content; the experiment was designed to investigate the relationships between crystal quality and variations in acceleration level, growth rate, and zone stability [1].

The HISA, composed of three Sundstrand QA-2000 sensors and an electronics package, is designed to detect and record transient and oscillatory accelerations. Table 1 lists HISA performance specifications. Data were recorded at both 1 Hz and 50 Hz sampling frequencies as averages of acceleration impulses over two sampling periods. They do not, therefore, represent instantaneous acceleration. The electronics package is such that positive and negative aver-

Table 1. HISA performance specifications, after Schoess [1]

parameter	performance
orientation range	three-axis orthogonal 10^{-6} to 10^{-2} g at 1 Hz 10^{-5} to 10^{-2} g at 50 Hz
accuracy resolution	$\pm(1\% \text{reading} + 0.00002)$ g $<1.0 \times 10^{-6}$ g at 1 Hz 8.7×10^{-6} g at 50 Hz
frequency response ($\pm 5\%$)	0.025 to 19.500 Hz
DC bias	none (AC output)
sample data rate	50 Hz, 1 Hz
communications	RS-422/ASCII format
size	$20.3 \times 9.7 \times 5.3$ cm (1.046 cm ³)
mass	1.8 kg
power	5.6 W (28 V)

ages were recorded separately. This recording technique resulted in twelve data files for each time period studied: $\pm x$, $\pm y$, and $\pm z$ data for both the 1 Hz and 50 Hz sampling rates.

3 Data Analysis

The HISA data files were provided by the NASA Acceleration Characterization and Analysis Project (ACAP). The data were in tabular form with the averaged acceleration values and sensor temperatures listed for each time mark. The temperature variation recorded by the system was not enough to warrant temperature corrections to the data [3]. A problem with the recording hardware responsible for the switch between the two sampling rates caused spurious values to be recorded approximately once a second in the 50 Hz data. We tested three methods to resolve this problem: replacing the spurious points with zero, with a "not-a-number" marker, and with the same value as the preceding data point. The three techniques showed similar results, and we chose to use the zero replacement method.

Our approach to the analysis of the HISA data follows the Acceleration Data Processing Guide developed at the Center for Microgravity and Materials Research. This guide was developed to assist low-g experimenters interested in accelerometer data in determining their data access and processing needs based on their knowledge of experiment and acceleration sensor location and of experiment sensitivity to acceleration [4]. We assessed the sensitivity of the float-zone indium crystal growth experiment based on computer modelling of the experiment [5-6]. Table 2 lists the sensitivity limits used in our analysis.

Table 2. Sensitivity limits used in analysis, after Alexander and Zhang [6]

frequency and magnitude ranges of interest	10^{-4} g for 10^{-2} to 0.1 Hz
maximum tolerable acceleration (steady)	10^{-3} g for 0.1 to 10 Hz
maximum tolerable acceleration (transient)	10^{-6} g
	10^{-3} g

Typically, sensitivity limits are used to determine what segments of an acceleration data base to analyze in conjunction with experimental results. Sections of accelerometer data in which the sensitivity limits are exceeded are selected using a threshold detection routine. A relatively limited amount of accelerometer data was recorded by the HISA during STS-32 (~10 megabytes representing ~5 discontinuous hours). Because of this, the entire data base was analyzed, with increased attention given to segments where the sensitivity limits were exceeded and where known acceleration sources were active.

A typical processing routine for residual acceleration data uses the basic techniques of time series and spectral analysis. These include calculating series statistics (mean, minimum, maximum, variance), plotting time histories of individual axes of data and vector magnitudes, and evaluating and plotting amplitude and power spectral densities to

investigate the frequency components present and their relative strengths [4, 7-9].

As mentioned in sect. 2, the HISA data were digitized so that positive and negative averages were recorded separately. This recording technique necessitated some specialized analysis. Because we are generally more interested in the magnitude of the acceleration vector at a location than in the individual axial acceleration readings, we used the six data files from each sampling frequency to form the vector magnitude, that is $|a| = \sqrt{(\pm a_x^2 + \pm a_y^2 + \pm a_z^2)}$, where $a = (\pm a_x, \pm a_y, \pm a_z)$ represents the positive and negative averages of the acceleration vector.

We transformed the HISA time histories into the frequency domain in a similar manner. Each of the six data files for each sampling rate was Fourier transformed to create the corresponding amplitude spectrum. To demonstrate that this technique is appropriate, we made a visual comparison of the spectra with spectra resulting from more standard data bases. For a more quantitative test, we processed data from the STS-40 flight of the Space Acceleration Measurement System (SAMS) to simulate the HISA sampling and averaging technique. The time and frequency domain magnitudes obtained with the resampled SAMS data were comparable to those obtained through our standard SAMS processing techniques.

The visual comparisons of the HISA results to other data bases and the SAMS simulated data show that the typical structural modes seen in orbiter accelerometer data were present in the HISA data. The lowest frequencies, unfortunately, are obscured to some extent by a remnant effect of the " \pm " digitization. The lowest frequency component resulting from a Fourier transformation of a time series is a representation of the mean value of the series. The " \pm " digitization of the HISA data creates an artificial non-zero mean that corrupts the mean represented in the corresponding spectrum. Because of this effect, we generally disregard the lowest spectral components calculated. For the shortest HISA data files (the various thruster firings), this results in a lower frequency limit of about 0.1 Hz.

4 HISA Data Plots

We present several characteristic examples from the HISA data base. Fig. 1 shows a time history and amplitude spectrum for 50 Hz data collected during a primary reaction control system firing. A high thrust pulse occurs about 5 s into the record, with possible lower magnitude thrusts occurring at about 45 and 90 s. The amplitude spectrum indicates that several orbiter structural modes are excited during this period, most notably in the 3, 5, 7, 10, and 13 Hz regions. The 17 Hz component, which is related to the Ku band antenna dither and a nearby orbiter structural mode, is excited. The lower magnitude, narrow band signals at 16 and 20 Hz are unusual, and at present their origin is uncertain. Early analysis of SAMS mid-deck data from STS-43, August 1991, suggests that the 20 Hz frequency may be a local, mid-deck structural or equipment-related excitation. Fig. 2 shows comparable plots for the 1 Hz data. Note that the amplitude spectrum plot can be used to

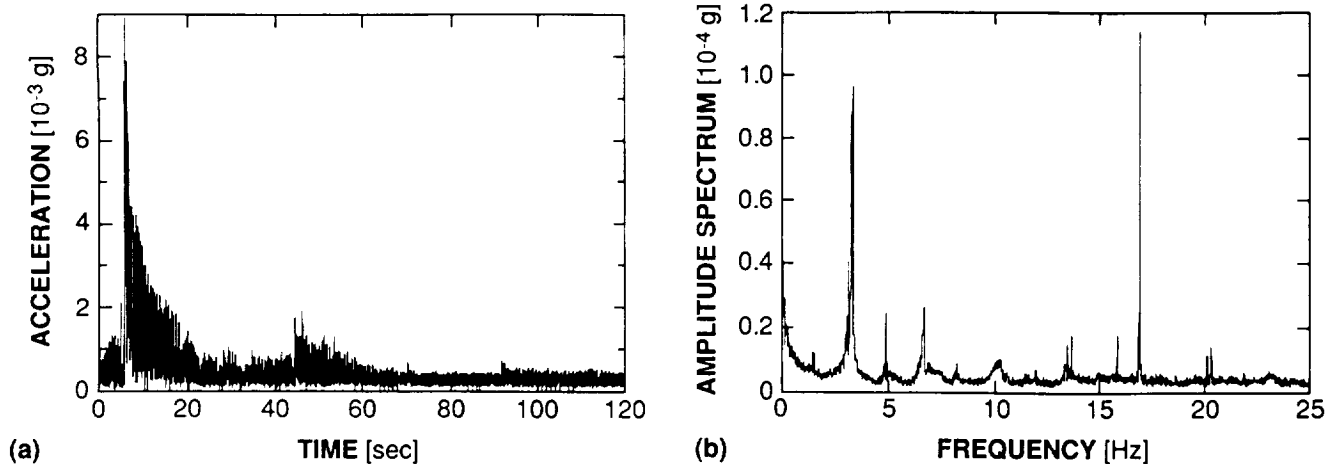


Fig. 1. Example of a primary reaction control system firing recorded by the HISA in the mid-deck of Columbia on STS-32. 50 Hz data. (a) acceleration vector magnitude. (b) combined amplitude spectrum

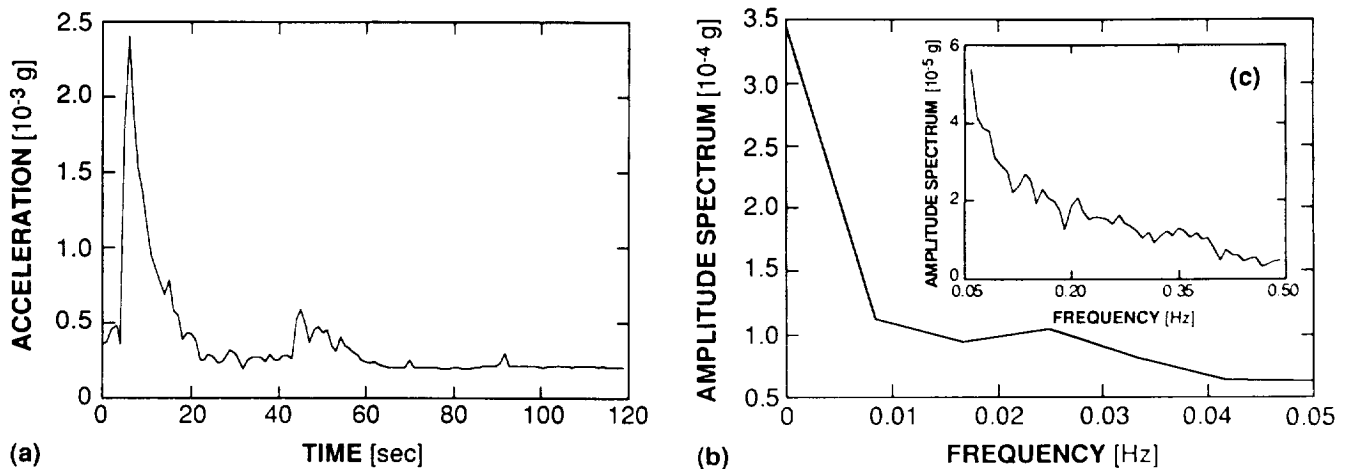


Fig. 2. Primary reaction control system firing shown in fig. 1, but as recorded by the HISA at 1 Hz sampling rate. (a) acceleration vector magnitude. (b) combined amplitude spectrum

supplement the lower frequency information obscured in fig. 1. Data recorded during an Orbiter Maneuvering System (OMS) burn are shown in fig. 3. The burn produces a short pulse-like acceleration response at the mid-deck location of the HISA. Structural modes in the 3.5 and 7 Hz range are excited.

Figs. 4–6 show HISA data collected during a period of crew exercise on the mid-deck treadmill. The treadmill was located approximately 2 m from the HISA. Fig. 4 shows a 1 Hz data window, and corresponding amplitude spectrum, collected during a crew treadmill exercise period. Note the high and low magnitude segments related to different exercise intensities. Fig. 5 shows 50 Hz data collected during a running or jogging (high intensity) exercise phase. Fig. 6 shows a segment from a less intense exercise stage, such as a walking or cool down period. Note that the overall acceleration level of fig. 6 is lower in magnitude than that of fig. 5. The most interesting aspect of these plots is the difference in the amplitude spectra. The spectra alone could be used to identify that the crew member was exercising at different levels of intensity.

This is explained as follows. The higher magnitude (running) segments of the treadmill data are dominated by a 2.7 Hz component, fig. 5. This frequency is related to an orbiter structural mode and is being driven by the footfalls of the crew member. In fig. 6, a slower exercise rate is represented (walking) and has a correspondingly lower frequency of footfalls. The 1.8 Hz component may be a higher harmonic of the 0.9 Hz component, or the two components may represent the crew member's upward and downward movements which differ in magnitude due to the treadmill restraint system. In this case, the 3.5 Hz structural mode is excited, possibly related to a doubling of the 1.8 Hz mode.

Because of the relatively small amount of data collected with the HISA during STS-32, we analyzed the entire data set, rather than limit the analysis based on sensitivity values given in table 2. Comparison of the HISA time histories to the limits in table 2 indicates that the transient time domain limit of $10^{-3} g$ was exceeded about 35% of the time as recorded at 50 Hz and 39% of the time at 1 Hz. The transient limit typically was exceeded during periods of

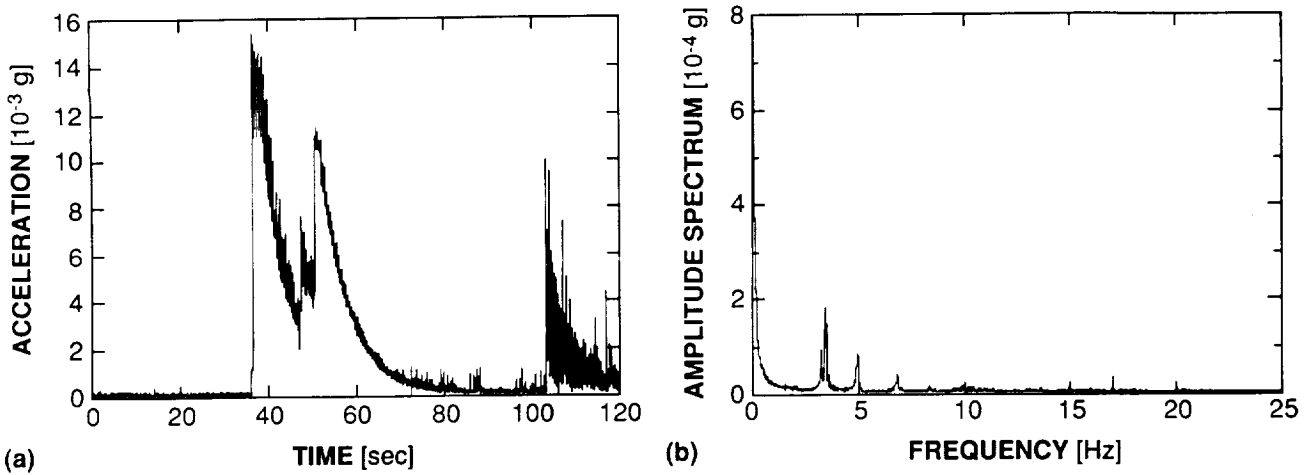


Fig. 3. Example of an orbiter maneuvering system firing recorded by the HISA in the mid-deck of Columbia on STS-32. 50 Hz data. (a) acceleration magnitude. (b) combined amplitude spectrum

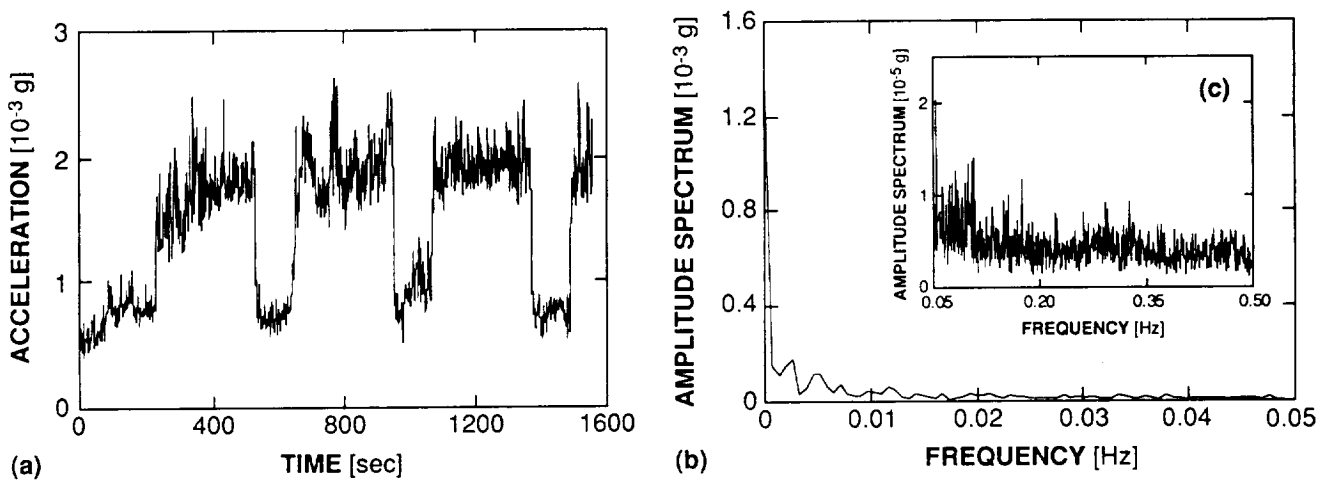


Fig. 4. Example of acceleration level during crew treadmill exercise period recorded by the HISA in the mid-deck of Columbia on STS-32. 1 Hz data. Note the different acceleration levels corresponding to different stages of the treadmill exercise protocol

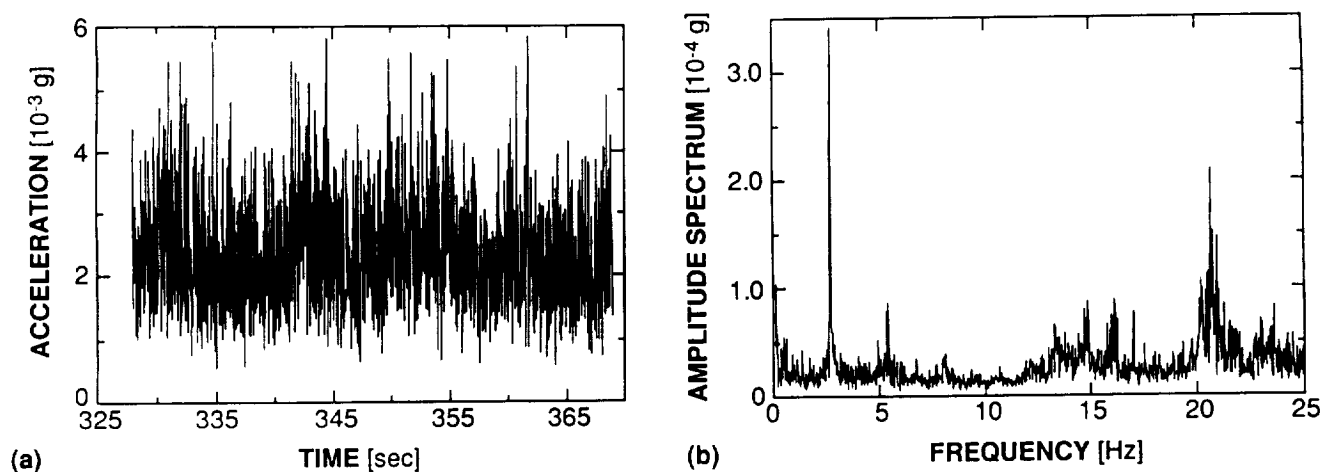


Fig. 5. Segment of 50 Hz data from higher magnitude section of fig. 3. (a) acceleration vector magnitude. (b) combined amplitude spectrum. Note the 2.7 Hz structural mode excited by footfall frequency

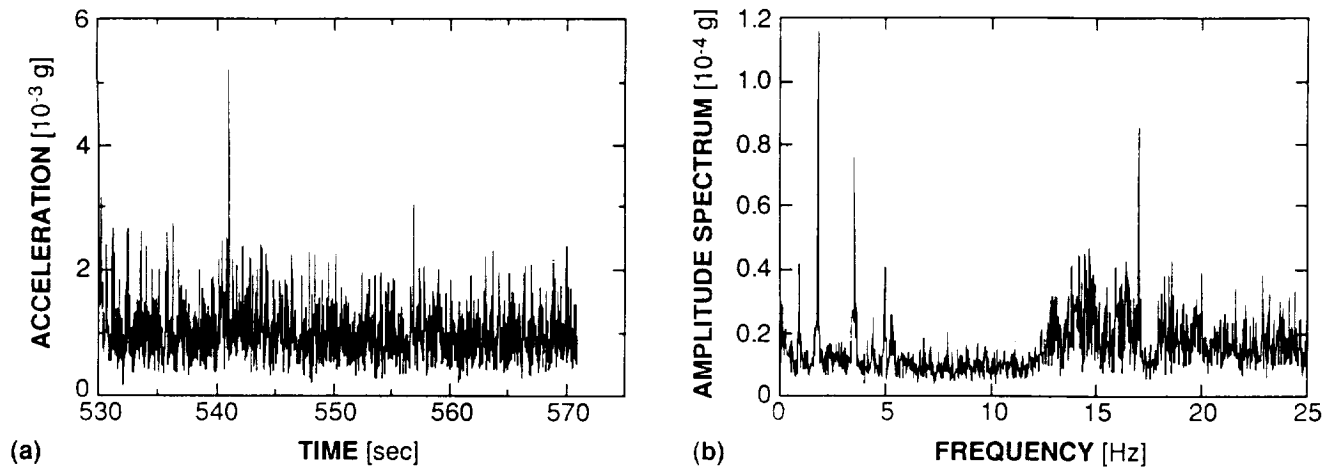


Fig. 6. Segment of 50 Hz lower magnitude section of fig. 3. (a) acceleration vector magnitude, (b) combined amplitude spectrum. Note the lower footfall frequency

crew exercise and orbiter maneuvers. The sampling frequencies used, the lengths of the time windows recorded, the limited amount of data storage capacity, and the analysis limitations related to the “ \pm ” digitization precluded the testing of the steady-state time domain limit. Note that the HISA was designed only to measure g -jitter (transient and oscillatory accelerations).

Evaluation of the frequency domain tolerance limits is particularly important in the case of float-zone experiments. These experiments involve a molten liquid zone suspended between two rods. The free surface of the zone will move if subjected to a disturbance. In particular, for vibrations, the zones tend to be most sensitive to disturbances with frequencies corresponding to eigenfrequencies of the bridge. For the case of an indium floating zone, these frequencies lie in the 0.1 to 10 Hz band [6]. For the HISA data analyzed, the maximum tolerable magnitude for this range was not exceeded. The 10^{-2} to 0.1 Hz frequency range limit in table 2 was not exceeded for segments of data during treadmill activity and quiet periods. The lowest frequencies of this range cannot be evaluated for the segments of thruster firings because the short time windows recorded impose a lower frequency analysis limit in the 10^{-2} Hz range. For frequencies above $2-3 \cdot 10^{-2}$ Hz, the sensitivity limit for zone breakage was not exceeded.

5 Discussion

The results obtained from processing the STS-32 *Honeywell* In-Space Accelerometer data are comparable in magnitude and character to the expanding orbiter low-gravity measurement data base. The HISA was one of the first systems to be used in the orbiter mid-deck and, consequently, the data should serve as a standard against which later results will be compared.

Acceleration vector magnitudes recorded by the HISA for primary reaction control system firings (figs. 1 and 2) are consistent with data recorded in the Spacelab module during the Spacelab 3 and Spacelab Life Sciences 1 missions and in the payload bay during STS-32 [7, 11, 12]. It should be noted, however, that in some cases the accelerations

exceed the accelerometer maximum range, so we do not know the actual maximum level of acceleration related to thruster firings.

As can be seen in all these data bases, the frequency components of a time segment of acceleration data are generally dominated by the various orbiter and Spacelab structural modes [4, 7–10]. For the case of acceleration data collected during crew treadmill exercise (figs. 4–6), vibration frequencies related to the crew member’s footfalls on the treadmill and subsequent pull on the restraint system are not only detectable in spectral representations, but are also seen to excite structural modes of the same or related frequencies. Analysis of HiRAP data reported in *Dunbar et al.* [11] indicates that the magnitude difference between exercise stages is translated to the orbiter payload bay at an overall reduced magnitude, but that the footfall frequencies are not evident. We interpret this as an indication that only the vibration of the excited structural modes propagates the distance 18 m between the treadmill and payload bay. The footfall source excites structures local to the mid-deck treadmill and HISA sensors.

Despite the fact that the HISA data are consistent with other data bases, we think that there are several aspects of the system that should be modified before future flights. We believe that the “ \pm ” digitization method is a relatively undesirable form of data conversion for storage. Modification of the electronics to allow recording of a single time series for each of the three orthogonal axes would alleviate several processing difficulties. Correction of the sampling rate switching problem would also obviate data replacement or filtering schemes and increase the number of meaningful data points available to the experimenter.

Acknowledgements

This work was funded by the National Aeronautics and Space Administration through contracts NAS8-36995, DO 126, and grant NAG8-759. Bonnie J. Dunbar and Donald A. Thomas, Astronaut Office, NASA Johnson Space Center, were Principal Investigators of the MDE. Dr. Dunbar was also Mission Specialist on STS-32 and was responsible for most of the MDE operations.

We would like to thank Charles R. Baugher, Marshall Space Flight Center, for providing us with the HISA data and funding for the processing and experiment modelling.

References

- 1 *Schoess, J. N.*: Honeywell In-Space Accelerometer STS-32 Final Report, Honeywell Technical Report, 1990
- 2 *Dunbar, B. J., Thomas, D. A., Schoess, J. N.*: The Microgravity Environment of the Space Shuttle Columbia Middeck During STS-32, NASA Technical Paper 3140, November 1991
- 3 *Schoess, J. N.*: Personal Communication
- 4 *Rogers, M. J. B., Alexander, J. I. D.*: Experimental Specific Processing of Residual Acceleration Data, 30th Aerospace Sciences Meeting, January 1992, AIAA Paper No. 92-0244
- 5 *Zhang, Y. Q., Alexander, J. I. D.*: Sensitivity of Liquid Bridges Subject to Axial Residual Acceleration, *Phys. Fluids A* 2 (1990) 1966–1974
- 6 *Alexander, J. I. D., Zhang, Y. Q.*: The Sensitivity of a Non-Isothermal Liquid Bridge to Residual Acceleration, in: *Microgravity Fluid Mechanics*, K. J. Rath (ed.), Springer Verlag, Berlin, 1992, 167–174.
- 7 *Rogers, M. J. B., Alexander, J. I. D.*: Analysis of Spacelab 3 Residual Acceleration Data, *J. Spacecraft and Rockets* 28 (1991) 707–712
- 8 *Rogers, M. J. B., Alexander, J. I. D., Snyder, R. S.*: Analysis Techniques for Residual Acceleration Data, NASA Technical Memorandum, NASA TM-103507, July 1990
- 9 *Rogers, M. J. B., Alexander, J. I. D.*: Cross-correlation Analysis of On-orbit Residual Accelerations in Spacelab, Proceedings of the 29th Aerospace Sciences Meeting, January 1991, AIAA Paper 91-0348
- 10 *Baugher, C. R.*: Early Summary Report of Acceleration Measurements for STS-40, October 1991
- 11 *Dunbar, B. J., Giesecke, R. L., Thomas, D. A.*: The Microgravity Environment of the Space Shuttle Columbia Payload Bay During STS-32, NASA Technical Paper 3141, November 1991
- 12 *Arnett, G.*: Spacelab-3 Low-g Accelerometer Data from the Fluid Experiments System (FES). In: Proceedings of the Measurement and Characterization of the Acceleration Environment On Board the Space Station, Guntersville, AL, August 1986, Paper 11

Appendix III

NUMERICAL SIMULATION OF THERMOCAPILLARY FLOW UNDER ZERO
AND LOW GRAVITY CONDITIONS

See
1250
JSA 28663

J. Iwan D. Alexander, H. Cordier, Y. Zhang
Center for Microgravity and Materials Research
University of Alabama in Huntsville, Huntsville Alabama

and
Jalil Ouazzani
Institute de Mécanique des Fluides de Marseille
Marseille, France

Abstract

This paper discusses the numerical solution methods and results of steady and unsteady thermocapillary (surface-tension) and buoyancy driven flows in 2-D cavities and liquid columns. The 2D cavity was assumed to be square with one free surface with a zero Capillary number (i.e. the free surface was constrained to be flat). A pseudospectral method was used to solve steady and unsteady surface tension-driven and mixed buoyancy-surface tension flows in a square cavity. For the liquid column a finite-difference scheme based on a Picard iteration was used to solve for the flow, temperature and free surface shape. The surface of the liquid column was allowed to deform and, as for the 2D cavity, the surface tension was assumed to depend on temperature.

Nomenclature

- L length of free surface
- N_r number of points in the radial direction
- N_z number of points in the axial direction
- Pr Prandtl number
- r radial coordinate
- Re surface Reynolds number
 ΔT temperature difference between the sidewalls of the square cavity- z axial coordinate
 γ_T rate of change of surface tension with respect to temperature- μ shear viscosity
- ν kinematic viscosity

I. Pseudospectral Method: Square Cavity

We assumed that a constant viscosity Boussinesq fluid was contained in a square cavity with differentially heated isothermal sidewalls, a lower adiabatic boundary and a flat upper surface at which motion was driven by gradients in (temperature dependent) surface tension. A Chebyshev

pseudo-spectral collocation method^{1,2} was used in conjunction with an influence matrix technique¹ to solve the problem in stream-function vorticity form. Results of the calculations were carefully compared to results obtained previously using finite difference³ and finite volume⁴ methods.

For steady flow, results of the comparison are presented in Table I for Reynolds numbers ($Re=L\Delta T\gamma_T/\mu\nu$) in the range $1000 < Re \leq 10^4$ and for Prandtl numbers, $Pr=\nu/\kappa$, in the range $10^{-2} < Pr < 1$. At $Re > 1000$, convergence was readily obtained for a given number of collocation points (grid size), but some effort had to be made to ensure grid convergence of solutions. This also appears to be the case for finite volume and finite difference methods applied to the same problem. We found that, up to $Re=10^4$, 41×41 collocation points were necessary to obtain a grid converged solution. That is the solution changed by less than 1% after increasing the number of collocation points by 50%.

The 2D surface tension-driven flow was also examined for its sensitivity to sinusoidal vibration. For a fixed vibration amplitude and frequency, our results show a decreased sensitivity with increasing Re. An important aspect of this part of our work again concerned the importance of using enough spatial resolution to capture the physics. We found for the vibration problem that unless a sufficiently fine grid was used (in some cases 65×65 collocation points) spurious oscillations were introduced. Spurious oscillations were not found to occur for the same vibration imposed on a closed cavity with the same temperature gradient. The importance of spatial resolution is also seen from our results for thermocapillary flow in liquid columns with deformable surfaces.

II. Liquid Columns: Centered Finite Differences

We approached the problem of computing steady free boundary problem for thermocapillary and buoyancy-driven flow in cylindrical liquid bridge using a Picard iterative procedure^{5,6} as since the location of the free liquid surface is *a priori* unknown: The iterative procedure is as follows:

Table I: Comparison of the results of our pseudospectral method (AC) with those of Zebib, Homsy and Meiburg (ZHM)³, Carpenter and Homsy (CH)⁴.

Re	AUTHORS	M × N	Nu ⁻	Nu ⁺	ψ × 10 ²
1000	ACO	17×17	1.915	1.932	0.481
	"	41×41	1.926	1.926	0.482
	"	65×65	1.926	1.926	0.482
	ZHM	62×54	1.93	1.92	0.479
2000	ACO	17×17	2.481	2.507	0.439
	"	41×41	2.474	2.474	0.433
	"	65×65	2.474	2.474	0.433
	ZHM	62×54	2.47	2.47	0.424
3000	ACO	17×17	2.920	2.921	0.426
	"	41×41	2.865	2.866	0.414
	ZHM	62×54	2.86	2.85	0.404
4000	ACO	17×17	3.288	3.255	0.415
	"	41×41	3.172	3.175	0.394
	ZHM	62×54	3.17	3.16	0.384
	ZHM	62×54	3.17	3.16	0.384
5000	ACO	17×17	3.603	3.542	0.403
	"	41×41	3.429	3.435	0.377
	"	65×65	3.435	3.434	0.377
	ZHM	65×65	3.459	3.448	0.370
	"	65×65	3.420	3.412	0.366
	"	80×80	3.428	3.425	0.369
6000	ACO	41×41	3.654	3.662	0.363
	ZHM	62×54	3.65	3.63	0.350
7000	ACO	17×17	4.112	4.026	0.382
	"	41×41	3.855	3.865	0.351
	"	65×65	3.861	3.862	0.351
	ZHM	62×54	3.85	3.83	0.337
10⁴	ACO	17×17	4.683	4.604	0.367
	"	41×41	4.361	4.375	0.323
	"	65×65	4.360	4.366	0.322
	ZHM	62×54	4.34	4.32	0.305
	CH	64×64	4.36	4.40	0.323

1. guess the free surface shape for the initial iterate;
2. obtain the approximate temperature and velocity fields by transforming the governing equations and boundary conditions to a circular cylindrical (r,z) domain via a non-orthogonal transformation and solve them using a pseudo-unsteady semi-implicit method;
3. obtain the pressure at the free surface by integrating the transformed momentum equation;
4. use the normal force balance condition at the free surface to decide how to update the free surface location;
5. return to step 2. Repeat until convergence is obtained by satisfying all equations and boundary conditions to a specified degree of accuracy.

The details of this numerical procedure are discussed in previous work⁶.

Apart from varying the iterative step size, convergence of the solution was checked by varying the spatial resolution of the mesh. This was particularly important at higher values of Re, where, owing to the space-centered-differences, the stream function was prone to exhibit "wiggles" if the grid Peclet number⁶ exceeded 2 in the vicinity of the disks. The wiggles are present for $N_r \times N_z = 26 \times 61$ and are not eliminated until $N_z = 101$. As observed by Ryskin and Leal⁷, an increase in the mesh resolution was found to eliminate this problem. We attempted to eliminate the wiggles and avoid the need for mesh refinement by employing second and third order upwind schemes for convective terms. We found that while the wiggles were certainly eliminated for $N_r \times N_z = 26 \times 61$, the mesh still needed to be refined in order to obtain grid convergence. Since the end result was the same, we concluded that the centered difference scheme was preferable. A mesh of $N_r \times N_z = 26 \times 51$ was found to be sufficient for the results presented here with Reynolds numbers in the range $0 < \text{Re} < 10000$.

We have used above method to examine the influence of various parameters on momentum and heat transport and meniscus shape. In addition, a favorable comparison for full and half zones has been made between the results obtained using the combined scheme and those of Hyer et al.⁸ who employed a finite element scheme.

Acknowledgements

This work was supported by the National Aeronautics and Space Administration through grant NAG8-724, and NAS8 36995-D.O. 126 and also by the State of Alabama through the Center for Microgravity and Materials Research and the Alabama Supercomputer Network.

References

¹C. Canuto, M. Y. Hussaini, A. Quarteroni and T.A. Zang, Spectral Methods in Fluid Dynamics (Springer-Verlag, Berlin, 1988).

²U. Ehrenstein and R. Peyret, Int. J. Num. Meth. Fluids 30 (1989) 427.

³B. M. Carpenter and G. M. Homsy, Phys. Fluids 2 A (1990)

⁴A. Zebib, G.M. Homsy and E. Meiburg, Phys. Fluids 28 (1990)

⁵J. M. Floryan, Appl. Mech. Rev. 42 (1989) 323-341.

⁶Y. Q. Zhang and J. I. D. Alexander, International J. of Numerical Methods in Fluids. 14 (1992) 197-216.

⁷G. Ryskin and L. G. Leal, J. Fluid Mech. 148 (1984) 1-17.

⁸J. Hyer, D.F. Jankowski and G.P. Neitzel, AIAA paper 90-0406, 28th Aerospace Science Meeting, Reno Nv, 1990.